Article

Site-specific substitution in atomically precise carboranethiol-protected nanoclusters and concomitant changes in electronic properties

Vivek Yadav[1], Arijit Jana[1], Swetashree Acharya[1], Sami Malola[2], Harshita Nagar[1], Ankit Sharma [3], Amoghavarsha Ramachandra Kini[1], Sudhadevi Antharjanam [4], Jan Machacek[5], Kumaran Nair Valsala Devi Adarsh [3]✉, Tomas Base[5]✉, Hannu Häkkinen [2]✉ & Thalappil Pradeep [1]✉

We report the synthesis of $[Ag_{17}(o_1\text{-CBT})_{12}]^{3-}$ abbreviated as Ag_{17}, a stable $8e^-$ anionic cluster with a unique $Ag@Ag_{12}@Ag_4$ core-shell structure, where o_1-CBT is *ortho*-carborane-1-thiol. By substituting Ag atoms with Au and/or Cu at specific sites we created isostructural clusters $[AuAg_{16}(o_1\text{-CBT})_{12}]^{3-}$ ($AuAg_{16}$), $[Ag_{13}Cu_4(o_1\text{-CBT})_{12}]^{3-}$ ($Ag_{13}Cu_4$) and $[AuAg_{12}Cu_4(o_1\text{-CBT})_{12}]^{3-}$ ($AuAg_{12}Cu_4$). These substitutions make systematic modulation of their structural and electronic properties. We show that Au preferentially occupies the core, while Cu localizes in the tetrahedral shell, influencing stability and structural diversity of the clusters. The band gap expands systematically (2.09 eV for Ag_{17} to 2.28 eV for $AuAg_{12}Cu_4$), altering optical absorption and emission. Ultrafast optical measurements reveal longer excited-state lifetimes for Cu-containing clusters, highlighting the effect of heteroatom incorporation. These results demonstrate a tunable platform for designing nanoclusters with tailored electronic properties, with implications for optoelectronics and catalysis.

Atomically precise nanoclusters (NCs) of coinage metals (Au, Ag and Cu), protected by various organic ligands, represent an intensely active category of functional nanomaterials, capturing significant attention of materials science and nanotechnology[1-4]. With diameters ranging typically between 1 and 3 nm, these NCs resemble molecules with electronic energy states transitioning from quasi-continuous bands to discrete orbitals[5]. This transition, a consequence of quantum confinement, endows NCs with distinctive chemical, photophysical and optical properties[1,6-9]. Notably, the monodisperse character of these NCs, with a precise structure and composition and the ability to adopt various atomic arrangements offer unprecedented insights into their structure-property relationships[10,11]. These NCs possess intriguing optical properties attributed to multiple optical absorption bands, luminescence, and X-ray radioluminescence, which find applications across diverse fields of optics, sensors, nonlinear optics, X-ray scintillation, biomolecular imaging and solar cells[12-20]. Coinage metals have a strong affinity for various protecting ligands including thiolates, selenolates, phosphines, hydrides, halides, and alkynes[21-25]. The selection and combination of these ligands play crucial roles in determining the structure, size and composition of the resulting NCs[26-28]. Thiolate

[1]DST Unit of Nanoscience (DST UNS) and Thematic Unit of Excellence (TUE), Department of Chemistry, Indian Institute of Technology, Madras, Chennai 600036, India. [2]Department of Physics and Chemistry, Nanoscience Center, University of Jyväskylä, FI 40014 Jyväskylä, Finland. [3]Department of Physics, Indian Institute of Science Education and Research Bhopal, Bhopal 462066, India. [4]Sophisticated Analytical Instruments Facility (SAIF), Indian Institute of Technology, Madras, Chennai 600036, India. [5]Department of Synthesis, Institute of Inorganic Chemistry, The Czech Academy of Science, Rez 25068, Czech Republic. ✉e-mail: adarsh@iiserb.ac.in; tbase@iic.acs.cz; hannu.j.hakkinen@jyu.fi; pradeep@iitm.ac.in

ligands form stable metal NCs due to strong binding via the metal-thiolate (sulfide) interface[1].

In comparison to the conventional organo-thiols, carborane-thiols have emerged as an interesting group of ligands with structurally robust backbone. Metal NCs with carborane ligands have been reported as sensors of nitro-aromatic vapors[29] and as materials exhibiting hypergolic activity[30,31]. Similar type of activity was not observed for organo-thiolate-stabilized metal clusters. Carboranes, more precisely dicarba-*closo*-dodecaboranes of general formula, $C_2B_{10}H_{12}$, with their 12-vertex nearly icosahedral structure, offer promising prospects for synthesizing metal NCs with tunable properties as they can be derivatized by almost any organic functional group (thiol, selenol, phosphine, alkyne, etc.) commonly used in metal NCs[32–35]. In general, carboranes are characterized by rigid, robust, three-dimensional architectures, with superior chemical and thermal stability, having distinct electronic structures, making them valuable for applications ranging from luminescent polymer materials to catalysts, drug synthesis, energy storage materials, and molecular nanomachines[36–39]. Carboranes possess tunable electronic properties influenced by their dipole moment and 3D pseudoaromatic character, distinguishing them from other organic compounds[40,41]. While there are reports on carborane-thiol stabilized metal clusters with luminescence properties, challenges remain in synthesizing tunable multimetallic clusters with precise positioning of heteroatoms in the shell[32–35,42].

Incorporating a precise number of hetero-metal atoms into NCs through alloying represents a promising approach for introducing synergistic effects aimed at enhancing ambient stability, catalytic activity, and other key properties[43–49]. Heteroatoms like Pt, Pd, Au and Cu have been effectively incorporated into various Ag-based NCs via co-reduction of metal ions, galvanic and antigalvanic exchange, and post-synthetic modifications[43,50–56]. The selection of metal components and ligands plays a critical role in regulating the quantity and distribution of dopant atoms, and influencing the overall atomicity and consequently the electronic structure of the NCs[26,54,57–59]. Precise spatial arrangement of metal dopants and the formation of heteronuclear bimetallic bonds influence the properties of NCs, particularly their optical characteristics. Furthermore, adding different metals to single-metal nanohybrid systems has been shown to enhance their nonlinear optical properties[60–62]. Synthesizing silver NCs of specific nuclearity, site-specific incorporation of other metals and high purity of the resulting systems pose persistent challenges. Several factors, such as acidity, solvent, temperature, light, metal precursor, and ligand of choice, profoundly influence the nuclearity, shape, and surface activity of these NCs[1,32,63,64]. In addition to conventional co-reduction methods yielding NCs with metal-thiolate interfaces, unconventional synthetic strategies such as solid-state gel-based synthesis, mechanical grinding, microwave irradiation, and metal exchange-induced size focusing have been employed. Furthermore, fast purification techniques utilizing desalting columns have been used to scale up the production of high-purity NCs[65–68]. An Ag_{17} core protected with 4-*tert*-butylbenzene-thiol was predicted commputationally[69], in view of the difficulties associated with crystallization, and upon Au incorporation, the structure was solved by single crystal X-ray diffraction (SC-XRD)[70].

Herein, we present a systematic study of incorporation of gold and copper heteroatoms into a carborane-thiol protected M_{17} NCs, starting from monometallic Ag_{17} to bimetallic $AuAg_{16}$ and $Ag_{13}Cu_4$ to trimetallic $AuAg_{12}Cu_4$ clusters. The X-ray crystal structure of Ag_{17} revealed two different positions in the metal kernel which were substituted with Au and Cu, resulting in significant changes in the luminescence properties of the resulting clusters. Comparative photophysical studies show that the inner metallic skeleton determines the emissive band gap and excited state carriers. Density-functional theory (DFT) calculations provided insights into the molecular orbitals responsible for their electronic transitions. Additionally, femtosecond and nanosecond transient absorption (fs-ns TA)

measurements were employed to further explore the excited state charge transfer and relaxation dynamics of the NCs. This work manifests an interesting class of isostructural NCs with site-specific optical properties and establishes that specific ligands allow the creation of a range of compositionally diverse clusters of the same nuclearity, with distinctly different properties.

Results and discussion
Synthesis and crystallization
The Ag_{17} cluster was synthesized through a single-step chemical reduction of mixed precursors composed of silver nitrate ($AgNO_3$), 1,2-bis(diphenylphosphino)ethane (DPPE) and *ortho*-carborane-1-thiol (o_1-CBT) in dichloromethane (DCM):methanol (MeOH) (9:5, v/v) solvent mixture using sodium borohydride ($NaBH_4$) as a reducing agent. The bimetallic $AuAg_{16}$ and $Ag_{13}Cu_4$ clusters were synthesized with chloroauric acid ($HAuCl_4$) and copper(I) chloride (CuCl) as metal sources. Trimetallic $AuAg_{12}Cu_4$ NC was synthesized using the mixture of all three starting precursors: $AgNO_3$, $HAuCl_4$, and CuCl. Other synthetic conditions remained identical as for the synthesis of Ag_{17}. Specific details of the synthetic procedures are presented in the Methods. Incorporation of Cu at the shell by precisely alloying all the four positions was much challenging for $Ag_{13}Cu_4$ and $AuAg_{12}Cu_4$. Initially, in the synthesis of Cu incorporated Ag_{17}, multiple peaks in ESI-MS corresponding to $Ag_{17-x}Cu_x$ ($x = 0$-4) were observed as shown in Supplementary Fig. 1 which was later overcome leading to pure $Ag_{13}Cu_4$ NC by optimising the quantities of precursors. Similarly, crude sample of the trimetallic cluster showed multiple peaks in ESI-MS as shown in Supplementary Fig. 2 where the final cluster was isolated by crystallization. The formation of these NCs was monitored using time dependent UV-Vis absorption spectroscopy, which showed the prominent absorption peak at 400 nm for Ag_{17} and $Ag_{13}Cu_4$ as well as 385 nm for $AuAg_{16}$ and $AuAg_{12}Cu_4$ after 15 h of reduction (Supplementary Figs. 3–6). Although DPPE did not constitute the outer ligand shell of these NCs, it played a significant role in the synthesis as neither of the products were observed in the absence of it (Supplementary Fig. 7). DPPE also played an important role in making counterions in the crystallization of the bimetallic $AuAg_{16}$ and $Ag_{13}Cu_4$ NCs. The formation of metal clusters assisted by phosphine has also been observed in refs. 71,72 We performed synthesis by replacing DPPE with PPh_4Br and nBu_4NF as stabilizing counter cations in which no NCs were observed. Single-crystals suitable for X-ray diffraction were obtained by slow diffusion of hexane (either from vapors or from an overlayer) into the concentrated DCM or DCM- acetonitrile (ACN) /chloroform ($CHCl_3$) mixture solutions of the clusters (Ag_{17}, $AuAg_{16}$ and $Ag_{13}Cu_4$) and slow evaporation of the DCM-MeOH solution, at 4 °C in the case of $AuAg_{12}Cu_4$. Optical microscopy images demonstrated hexagonal, cuboidal, rod-like, and polyhedral crystals of Ag_{17}, $AuAg_{16}$, $Ag_{13}Cu_4$ and $AuAg_{12}Cu_4$ clusters (Supplementary Fig. 8), respectively. Surface morphology of each crystal was further investigated using field emission scanning electron microscopy (FE-SEM), and elemental composition was analyzed by EDS (see Supplementary Figs. 9–12).

Structural details resolved through SC-XRD
The SC-XRD analysis identifies the crystal system and space groups of the clusters. The Ag_{17} and $Ag_{13}Cu_4$ clusters were crystallized in orthorhombic and triclinic crystal systems in space groups Pbcn and P-1, respectively. $AuAg_{16}$ and $AuAg_{12}Cu_4$ clusters crystallized in trigonal and cubic crystal systems of space groups R-3 and Fd-3, respectively (crystallographic details are presented in Supplementary Tables 2–6). Optical anisotropy was also observed when the crystals were placed between cross-polarizing filters in the optical microscope where Ag_{17}, $AuAg_{16}$ and $Ag_{13}Cu_4$ show distinct change in color whereas $AuAg_{12}Cu_4$, being cubic, does not show any polarization (Supplementary Fig. 8).

The crystal structure of Ag_{17} reveals a metal core featuring three distinct positions, with a central atom surrounded by twelve Ag atoms
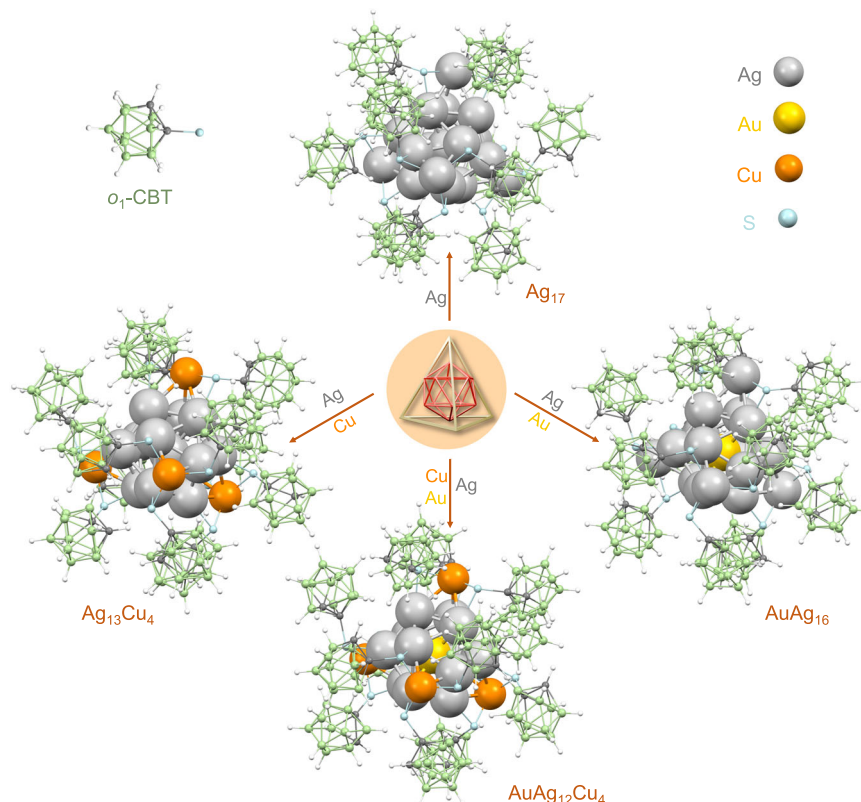
Fig. 1 | Elucidation of systematic synthesis and molecular architectures of isostructural Ag_{17}, $AuAg_{16}$, $Ag_{13}Cu_4$ and $AuAg_{12}Cu_4$ clusters shielded by o_1-CBT ligands. Systematic synthesis and molecular structures of isostructural Ag_{17}, $AuAg_{16}$, $Ag_{13}Cu_4$ and $AuAg_{12}Cu_4$ clusters, protected by twelve o_1-CBT ligands (metallic gray: silver, yellow: gold, reddish orange: copper, cyan: sulphur, green: boron, dark grey: carbon and white: hydrogen). The tetrahedral framework, built on an icosahedron is shown at the center.

forming an icosahedron and capped with four Ag atoms in a tetrahedral fashion (as depicted in Supplementary Fig. 13). Strong intermetallic bonding having an average Ag-Ag distances of 2.930 Å was observed in the metallic kernel. We note that the Ag-Ag distance in bulk silver metal is 2.89 Å. The structure offers three distinct positions for Ag within the Ag_{17} NC, simply understood as $Ag@Ag_{12}@Ag_4$, making it possible for the synthesis of bimetallic and trimetallic NCs. Introduction of Au in the reaction vessel results in $AuAg_{16}$, where Au occupies the central position ($Au@Ag_{12}@Ag_4$), while introduction of Cu results in $Ag_{13}Cu_4$, where the tetrahedral positions are occupied by Cu ($Ag@Ag_{12}@Cu_4$). In the case of trimetallic $AuAg_{12}Cu_4$ NC, both Au and Cu occupy their respective positions as central atom and outer tetrahedral positions, while Ag occupies the icosahedral positions ($Au@Ag_{12}@Cu_4$), as illustrated in Fig. 1.

All the four NCs are enveloped by twelve o_1-CBT ligands, where each carborane is connected with tetrahedral and icosahedral metal atoms through μ_2 sulfide linkages with an average metal-S distance of 2.495, 2.515, 2.385 and 2.339 Å for Ag_{17}, $AuAg_{16}$, $Ag_{13}Cu_4$ and $AuAg_{12}Cu_4$ clusters, respectively (Supplementary Fig. 14). The average intermetallic distances of the central icosahedral M_{13} inner kernel was 2.938 Å for Ag_{17}; 2.931 and 2.930 Å for $AuAg_{16}$ and $Ag_{13}Cu_4$, respectively; and 2.902 Å for $AuAg_{12}Cu_4$, as presented in Supplementary Fig. 14. Contraction of the icosahedral core of Ag_{17} was observed for $AuAg_{16}$ and $Ag_{13}Cu_4$, which was further contracted for $AuAg_{12}Cu_4$ making it the highest symmetrical structure. The centred icosahedral Ag_{13} kernel of $M_{17}S_{12}$ atomic arrangement resembles the seven or eight Ag(I) ions capping of the Ag_{13} kernel, forming the M_{20} and M_{21} clusters. Comparison of different dopped systems of M_{20} or M_{21} with M_{17} systems shows site specificity of the M_{17} system where the nuclearity, type of ligands as well as the definite composition remain intact for the bimetallic as well as trimetallic clusters (Supplementary Fig. 15)[73–77].

The unit cell molecular packing of $AuAg_{16}$ and $Ag_{13}Cu_4$ as presented in Supplementary Fig. 16 reveals that certain fragments, namely, $[Au(DPPE)_2]^+$ and $[Cu(DPPE)_2]^+$, were crystallized along with the NCs. The distance of $[Au(DPPE)_2]^+$ and $[Cu(DPPE)_2]^+$ fragments from the respective central metal atom of NC is ≈13 Å (Supplementary Fig. 16). The existence of non-covalent interactions such as, C-H...π and B-H...π, between the fragments and NCs are the key features in the crystal lattice of $AuAg_{16}$ and $Ag_{13}Cu_4$ which assist in holding the molecules together in their crystal lattice (Supplementary Fig. 17). Additionally, B-H...π interactions between the carboranes gives stabilization to the crystal lattice of all the NCs. Figure 2 and Supplementary Fig. 18 indicating lamellar packing of the NCs within the lattice. The cluster $AuAg_{12}Cu_4$ crystallizes in the cubic system which also shows pores but the void size and porosity are not well defined as the counter ions are not evident in the SC-XRD structure as shown in Supplementary Fig. 19.

Mass spectrometric investigations

High-resolution electrospray ionization mass spectrometric (HR-ESI-MS) studies were performed to verify the molecular compositions of these clusters. Negative ion mode ESI-MS spectrum of Ag_{17}, $AuAg_{16}$, $Ag_{13}Cu_4$ and $AuAg_{12}Cu_4$ clusters showed prominent peaks at m/z 1312.42, 1342.11, 1253.48, and 1283.15, respectively (Fig. 3a). All these peaks have (3-) charge making the overall masses as 3937.26, 4026.33, 3760.44, and 3849.45 amu, which correspond to the Ag_{17}, $AuAg_{16}$, $Ag_{13}Cu_4$ and $AuAg_{12}Cu_4$ clusters, respectively, with their ligands showing exact mass differences between the respective NCs. The isotopic distribution of the experimental peak matches well with the simulated spectrum (inset of Fig. 3a). The initially synthesised crude samples of $Ag_{13}Cu_4$ and $AuAg_{12}Cu_4$ NCs showed multiple peaks in the negative mode ESI-MS (Supplementary Figs. 1, 2) which were later
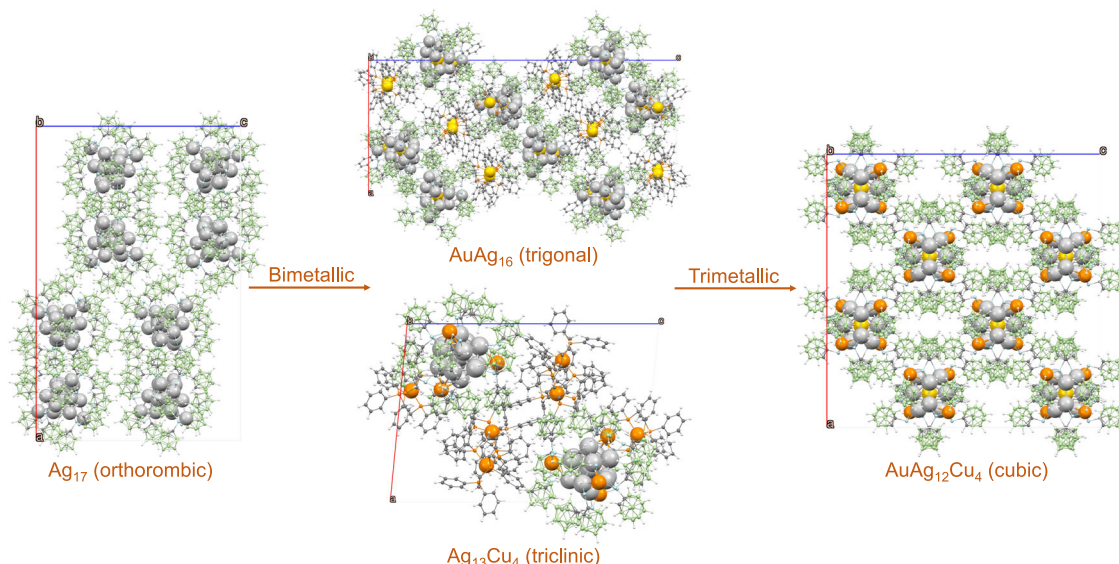
Fig. 2 | Supramolecular packing of the monometallic Ag_{17}, bimetallic $AuAg_{16}$ and $Ag_{13}Cu_4$, and trimetallic $AuAg_{12}Cu_4$. Ag_{17} are packed in an orthorhombic system. When Au and Cu are incorporated, the resulting bimetallic clusters $AuAg_{16}$ and $Ag_{13}Cu_4$ are packed in trigonal and triclinic systems, respectively. The trimetallic $AuAg_{12}Cu_4$ cluster, packed in a cubic system, exhibits the most symmetrical packing (metallic gray: silver, yellow: gold, reddish orange: copper, cyan: sulphur, green: boron, dark grey: carbon, orange: phosphorous and white: hydrogen).

eliminated by optimising precursor quantities and crystallization, respectively. Collision energy dependent MS/MS fragmentation of the selected molecular ion peaks were performed to get additional molecular insights of the clusters. The selected peak at m/z 1312.42 for the Ag_{17} cluster reveals that by incrementally increasing the collision energy (CE) from 0 to 15 (in instrumental units), two additional peaks emerge at m/z 1740.04 and 458.17, attributed to $[Ag_{16}L_{10}]^{2-}$ and $[AgL_2]^-$ species (as depicted in Supplementary Fig. 20). In the case of $AuAg_{16}$, at a CE of 15, the appearance of two new peaks at m/z 1784.06 and 458.17 implies the generation of $[AuAg_{15}L_{10}]^{2-}$ and $[AgL_2]^-$ fragments, respectively (Supplementary Fig. 21). Upon increasing the CE to 25, two peaks were detected at m/z 1672.72 and 414.27, due to $[Ag_{13}Cu_3L_{10}]^{2-}$ and $[CuL_2]^-$ species, respectively (Supplementary Fig. 22). Similarly, for the trimetallic $AuAg_{12}Cu_4$ cluster, peaks appeared at m/z 1717.28 and 414.27 at CE 25 due to $[AuAg_{12}Cu_3L_{10}]^{2-}$ and $[CuL_2]^-$, respectively (Supplementary Fig. 23). The emergence of $[ML_2]^-$ fragments with M representing either Ag in Ag_{17} and $AuAg_{16}$ or Cu in $Ag_{13}Cu_4$ and $AuAg_{12}Cu_4$, distinctly illustrates the peripheral environments characteristic of these clusters (Fig. 3b, Supplementary Figs. 20–23). In our earlier reports, comparable patterns of systematic fragmentation of surface carborane and carborane-thiolates were noted in Ag_{42} and Ag_{21} clusters[32,35]. The clusters did not show features in the positive-ion mode. However, the characteristic ion peak at m/z 993.24 and 859.20 in positive-ion mode confirms the presence of $[Au(DPPE)_2]^+$ and $[Cu(DPPE)_2]^+$ as counterions in the crystals of $AuAg_{16}$ and $Ag_{13}Cu_4$, respectively. However, both the ions were seen in the mass spectrum of the as synthesized crude of $AuAg_{12}Cu_4$ but detailed analysis of the crystal structure and the positive mode ESI-MS of the crystals confirmed their absence in the crystals (Supplementary Figs. 24, 25). Such complex counter cations like $[Ag(DPPE)_2]^+$, $[Au(DPPE)_2]^+$ and $[Cu(DPPE)_2]^+$ were not observed in the case of Ag_{17} and $AuAg_{12}Cu_4$ in the SC-XRD as well as in the ESI-MS measurements and we propose that Na^+ derived from $NaBH_4$ could be the plausible counterion. Therefore, the complete compositions have been identified as $[Na^+]_3[Ag_{17}(o_1-CBT)_{12}]^{3-}$, $[[Au(DPPE)_2]^+]_3[AuAg_{16}(o_1-CBT)_{12}]^{3-}$, $[[Cu(DPPE)_2]^+]_3[Ag_{13}Cu_4 (o_1-CBT)_{12}]^{3-}$ and $[Na^+]_3[AuAg_{12}Cu_4(o_1-CBT)_{12}]^{3-}$ for Ag_{17}, $AuAg_{16}$, $Ag_{13}Cu_4$ and $AuAg_{12}Cu_4$, respectively. Crystallization of the NCs using PPh_4^+ and nBu_4N^+ as counter cations was also tried where the clusters degraded and eventually no crystals were formed.

Additional characterization

The UV-Vis absorption spectra of the NCs in DCM show distinct characteristic features (Fig. 3c–f). Strong and relatively sharp absorption bands were observed: Ag_{17} exhibits bands at 400, 312, 269, and 241 nm; $AuAg_{16}$ at 385, 288, and 271 nm; $Ag_{13}Cu_4$ at 475, 400, and 307 nm; and $AuAg_{12}Cu_4$ at 385, 303, and 265 nm. These features signify the closely-spaced molecule-like electronic states within these NCs. The major absorption bands centered at 400 nm for Ag_{17} and $Ag_{13}Cu_4$ shift to 385 nm for $AuAg_{16}$ and $AuAg_{12}Cu_4$, attributed to the electronic perturbation of the cluster upon single Au atom substitution in the center of the icosahedral framework. Stability over 2 months of the clusters in the solution was observed, which is demonstrated by identical UV-Vis absorption features (Supplementary Fig. 26).To further explore the thermal stability, UV-Vis spectra as well as the real time ESI-MS were collected after subjecting microcrystalline powder samples (8–10 mg) to heating at various temperatures for 90 min. All characteristic absorption features (Supplementary Figs. 27–30) remained without any change, which indicates high structural robustness of these clusters. They were stable up to 125, 150, 175, and 100 °C for Ag_{17}, $AuAg_{16}$, $Ag_{13}Cu_4$, and $AuAg_{12}Cu_4$, respectively. We see stability enhancement from Ag_{17} to bimetallic $AuAg_{16}$ and $Ag_{13}Cu_4$ but not in the trimetallic $AuAg_{12}Cu_4$. Thermogravimetric analysis (TGA) (Supplementary Figs. 31–34) revealed no discernible weight loss up to 125 °C for the clusters. As previously observed, carborane-thiol ligands have once again provided remarkable stability to the NCs. The exceptional stability of NCs with site-specific alloying protected by carborane-thiols aligns well with earlier reports, reinforcing their effectiveness in stabilizing these systems[35,78].

The X-ray photoelectron spectra of the four clusters, depicting peaks corresponding to all the anticipated elements, are presented in Supplementary Fig. 35. A more detailed examination of the metallic components within the NCs is presented in Supplementary Fig. 36. Specifically, the detailed spectra of Ag 3d reveal the existence of silver in two distinct oxidation states within Ag_{17}, $AuAg_{16}$ and $Ag_{13}Cu_4$. However, in the case of the $AuAg_{12}Cu_4$ NC, Ag is in zero oxidation state with a binding energy of 368.26 eV. Furthermore, the central Au atom is in its zero oxidation state in both $AuAg_{16}$ and $AuAg_{12}Cu_4$. Cu is detected in the clusters, $Ag_{13}Cu_4$ and $AuAg_{12}Cu_4$ (931.3 eV) in the oxidation state close to 1+. Notably, all the NCs exhibit sulfur in the
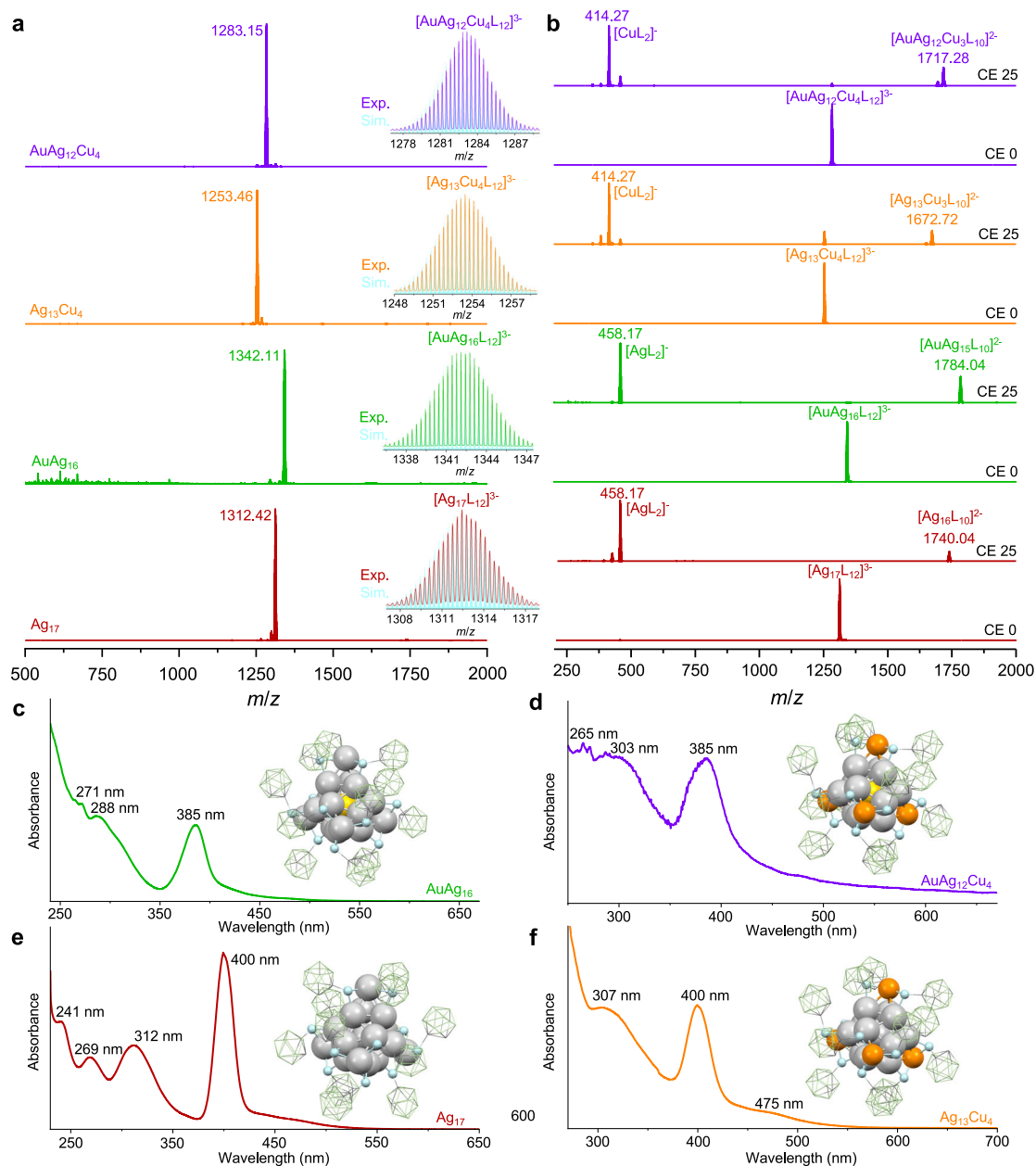
Fig. 3 | Comprehensive characterization of Ag$_{17}$, AuAg$_{16}$, Ag$_{13}$Cu$_4$ and AuAg$_{12}$Cu$_4$ clusters showing the comparative mass spectrometry, MS/MS fragmentation and UV-Vis absorption spectra. a Full range mass spectrum of all the four clusters. Inset shows the exact matching of the isotopic distributions of the experimental and simulated spectra (all simulated spectra are in cyan colour). **b** MS/MS fragmentation of the respective clusters at CE 0 and 25 showing the dissociation of surface ML$_2$ fragments (L: o_1-CBT). UV-Vis absorption spectra of **e** Ag$_{17}$ and **c** AuAg$_{16}$, **f** Ag$_{13}$Cu$_4$ and **d** AuAg$_{12}$Cu$_4$ clusters measured in DCM. Insets of **c−f** show the structures of the respective clusters (metallic gray: silver, yellow: gold, reddish orange: copper, cyan: sulphur, green: boron and dark grey: carbon).

thiolate form, along with two types of boron, originating from the carborane ligands (Supplementary Fig. 37).

To further investigate the ligand shell, FT-IR spectra of all the NCs were compared with that of the free o_1-CBT ligand (Supplementary Fig. 38). Typical vibration bands were observed in all the spectra confirming the presence of carboranes with their terminal BH bonds in the NCs. Two BH stretching vibration bands in free o_1-CBT at 2601 and 2573 cm^{-1} were shifted to a single band at a lower frequency of 2561 cm^{-1} upon binding to the NCs. This shift in the spectra of the NC-bound o_1-CBT ligand can be assigned to the effect of heavy substrate atoms, the molecule is anchored to, and to the general effect of space restriction within the packed surface, both of which affect the vibrational modes. The observed lower wavenumber of the ν_{BH} band in the

NCs thus matches with the formation of chemically bound thiolate moieties.

DFT investigations of substitution

DFT calculations were used to study the energetics of different sites for Au and Cu to get insights into the relative stability of the experimentally crystallized structures (for details, see the Methods). We investigated the cluster system with single Au and Cu substitutions using experimentally determined structure of the Ag$_{17}$ cluster. Heteroatoms were added in all the symmetrically different metal atom positions. Optimized structures and their relative energies are presented in Supplementary Fig. 39. Based on energies, Au favors the central site of the icosahedral metal core by 0.34–0.37 eV, in comparison to the
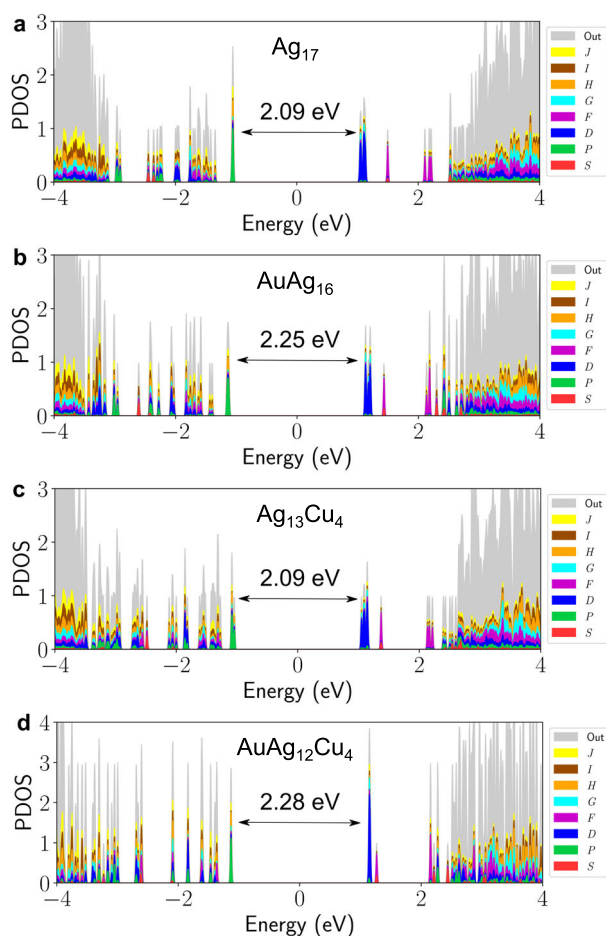
Fig. 4 | Comparative projected electronic density of states (PDOS) of the clusters. a–d The HOMO-LUMO energy gap of each cluster is centered around zero and the magnitude of the gap is presented. The Au-incorporated clusters, $AuAg_{16}$ and $AuAg_{12}Cu_4$, manifest the most substantial HOMO-LUMO gaps, measuring 2.25 and 2.28 eV respectively whereas the Ag_{17} and $Ag_{13}Cu_4$ clusters display band gaps of 2.09 eV.

capping sites of the outer kernel. Positions at the outermost metal layer, i.e., at the metal-thiolate interface, are the most unstable ones with 0.71 eV higher energy compared to the cluster with a gold atom in the center. The most stable cluster also seems to maximize the HOMO-LUMO gap (2.19 eV) from all the calculated systems, being ≈0.1 eV larger than for the other model structures. This structural and electronic stability, in comparison to the other sites, confirm the experimental observation of single Au-dopant in the center of the cluster.

Copper shows the opposite behavior than gold, i.e., energetically preferred sites are in the outermost metal-ligand interface, within the $Cu\text{-}(SR)_3$ surface motifs as presented in Supplementary Fig. 40. The rest of the possible sites in the metal core are 0.38–0.40 eV higher in energy. Considering the symmetry of the metal-ligand interface, there are exactly four energetically favorable sites in the metal-ligand interface which follow tetrahedral arrangement. This matches well with the experimental observation of exactly four Cu-dopants crystallized in the bi- and trimetallic clusters. The energetically stable Cu-substituted cluster model, similarly to the one with a Au atom in the center, has slightly larger (increase of 0.05–0.08 eV) HOMO-LUMO gap (2.05 eV) compared to the other calculated cluster models. This means that in both the cases the energetically stable structure is also electronically stable. Seemingly, the calculated energy difference is large enough to affect selectively the molecular composition and structure of the final cluster products. Similar behaviour of the

electronically preferred position of copper and gold was also observed for the MAg_{20} system having an icosahedral core[79].

DFT calculations of optical absorption properties

The electronic structures of these clusters were analyzed by projecting the density of states to spherical harmonic functions centered at the center of mass of the cluster which reveals the positions and symmetries of the superatom states. The results of this analysis are presented in Fig. 4. All clusters show the 8e⁻-superatom characteristics, the highest occupied states being of *P*-symmetry and the lowest unoccupied states of *D*-symmetry. Au-incorporated clusters, $AuAg_{16}$ and $AuAg_{12}Cu_4$ have the largest HOMO-LUMO gaps of 2.25 and 2.28 eV, whereas Ag_{17} and $Ag_{13}Cu_4$ clusters have 2.09 eV as the band gap. Distribution of the states vary slightly below the *P*-symmetric states between −1.5 and −3.5 eV, which is the region for metal-ligand interface states. Analysis of the electronic structure primarily suggests that the optical gap and dipole-allowed first transitions between HOMO *P*-states and LUMO *D*-states are potentially located similarly in Ag_{17} and $Ag_{13}Cu_4$, and would be found at slightly shorter wavelengths for $AuAg_{16}$ and $AuAg_{12}Cu_4$. The experimental band gap was estimated using differential pulse voltammetry (Supplementary Fig. 41) and the Tauc plot method. The Tauc plot analysis reveals experimental band gaps of 2.12, 2.25, 2.08, and 2.26 eV for Ag_{17}, $AuAg_{16}$, $Ag_{13}Cu_4$, and $AuAg_{12}Cu_4$, respectively (Supplementary Fig. 42), closely matching the theoretical values.

Theoretical UV-Vis absorption spectra of the clusters were calculated using the linear response time-dependent density-functional theory (LR-TDDFT). A comparison of the calculated and experimental UV-Vis spectra for all the clusters is presented in Fig. 5. More detailed comparison of the band positions is presented in Supplementary Table 1. For all these clusters, the first feature in the spectrum has relatively low intensity compared to the most prominent second band. Both experimental and computational spectra of Ag_{17} and $AuAg_{16}$ clusters are in good agreement across the measured spectrum. In the calculated spectra, the main bands are at 396 and 391 nm for Ag_{17} and $AuAg_{16}$, respectively while the corresponding experimental positions are 400 and 385 nm. A blueshift upon Au incorporation was observed in both experimental and theorical spectra. The two lowest energy bands in the spectra of $Ag_{13}Cu_4$ and $AuAg_{12}Cu_4$ are also present, but the calculated main peaks at 428 and 423 nm seem to be red-shifted by ≈0.2 eV, compared to the experiments. The first peak determining the optical gap is in agreement with the HOMO-LUMO gap. For Ag_{17} and $Ag_{13}Cu_4$, the first peak appears at 492 and 499 nm, respectively, whereas for the Au-incorporated clusters $AuAg_{16}$ and $AuAg_{12}Cu_4$, the peaks are at slightly lower wavelengths, 458 and 477 nm. This coincides with the corresponding HOMO-LUMO gap. The overall shape of the calculated spectra of Cu substituted clusters at lower wavelengths is however richer and more pronounced than the measured spectra. The trend with respect to incorporation of the cluster with Au-atom remains the same: the main peak is observed at a lower wavelength for the clusters with Au than without it, i.e., Ag_{17} compared to $AuAg_{16}$ and $Ag_{13}Cu_4$ compared to $AuAg_{12}Cu_4$. The clusters shown in Fig. 5c, d exhibit numerous "place-isomers" in solution due to mixing of metals at various core positions, driven by entropy. Calculations based solely on a single, "frozen" crystal structure may not fully capture the spectral properties observed experimentally in solution, leading to deviations between calculated and measured spectra in Fig. 5c, d. The excitations of all clusters create an oscillating electron density (as visualized in Fig. 5 insets) at the metal core and at the metal-ligand interface, but they does not reach the carborane ligands.

To analyze the spectral features, we calculated the dipole transition contribution maps (DTCMs) that show the strengthening and screening contributions in Kohn-Sham basis at the energy of the selected absorption band. The analysis is based on the perturbation time-dependent density-functional theory and was done for the Ag_{17}
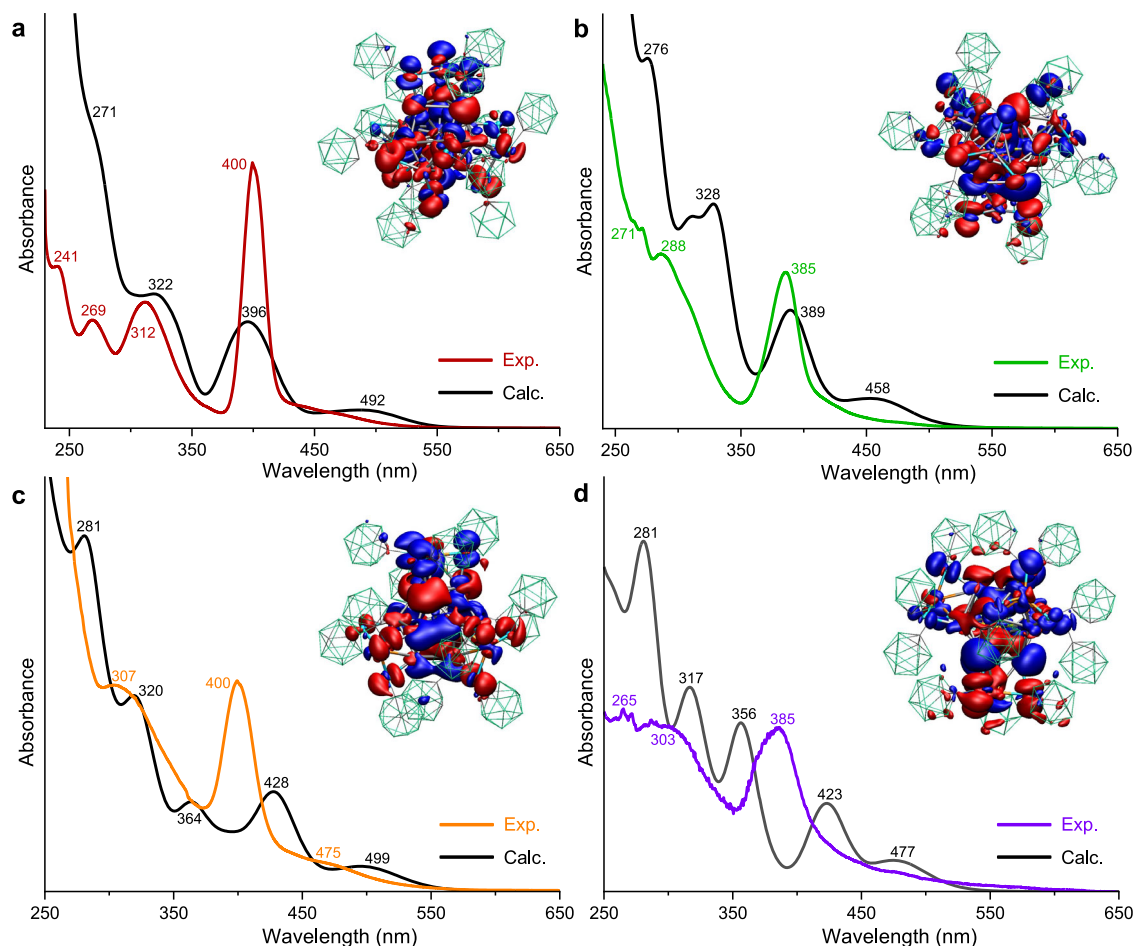
Fig. 5 | Comparison of calculated and experimental UV-Vis spectra with induced density inset for Ag_{17}, $AuAg_{16}$, $Ag_{13}Cu_4$ and $AuAg_{12}Cu_4$ clusters. Comparison of calculated and experimental UV-Vis spectra for **a** Ag_{17}, **b** $AuAg_{16}$, **c** $Ag_{13}Cu_4$, and **d** $AuAg_{12}Cu_4$. As two spectra are compared, absorbance is plotted in arbitrary units. Major peak positions are marked. Inset figures show the induced density (i.e., electron density oscillations, where red and blue are the positive and negative isosurfaces, respectively) for the excitations related to the peaks at **a** Ag_{17}: 396 nm, **b** $AuAg_{16}$: 389 nm, **c** $Ag_{13}Cu_4$: 428 nm and **d** $AuAg_{12}Cu_4$: 423 nm.

cluster as a reference system. The results are presented in Supplementary Fig. 43 and they confirm that the dipole-allowed transitions between superatom states P and D are mainly controlling the first two features in the spectrum. The highest wavelength peak is purely $P \to D$ transitions, while for the second main peak, the $P \to D$ transitions have been coupled with metal-ligand interface $\to D$-state type transitions. At even lower wavelengths, the bands change due to new transitions. These include transitions from superatom P states to higher unoccupied states (2.5–3.0 eV) and from states in the metal d-band region to unoccupied superatom D states. This analysis shows that superatom P and D states play a crucial role in the optical response, appearing throughout the wavelength range as starting or target states. For Cu-incorporated clusters, the red shift in the main peaks compared to Ag_{17} and $AuAg_{16}$ clusters is due to differences in the coupling between $P \to D$ transitions and metal-ligand interface $\to D$ transitions.

Photoluminescence properties

The photoluminescence (PL) properties of these clusters are studied in solution (in DCM) and solid states. Ag_{17} and $AuAg_{16}$ clusters emit weak luminescence in solution (insets of Fig. 6a, b). However, $Ag_{13}Cu_4$ and trimetallic $AuAg_{12}Cu_4$ clusters emit bright red and yellowish-orange emissions in solution (insets of Fig. 6c, d respectively). PL spectral measurement of Ag_{17} shows a very weak emission band at 650 nm upon a characteristic excitation centered at ≈400 nm. For centrally Au incorporated cluster, we observed a week emission band in the visible region (at 610 nm) and a prominent NIR emission band at ≈815 nm. The

absolute quantum yields of $Ag_{13}Cu_4$ and trimetallic $AuAg_{12}Cu_4$ clusters in DCM (using an excitation wavelength of 380 nm) were 5.80% and 4.37%, respectively. Quantum yields were below 0.1% for weekly emissive Ag_{17} and $AuAg_{16}$ clusters. We also observed significant emission enhancement upon cooling the Ag_{17} and $AuAg_{16}$ cluster samples to 77 K due to the rigidification-induced structural modification as presented in Fig. 6e, f. Bright luminescence was observed for Ag_{17} and $AuAg_{16}$ upon crystallization as well (Supplementary Fig. 44). Detailed structural analyses revealed robust intermolecular noncovalent interactions, specifically BH···BH, CH···BH, and BH···π interactions, within Ag_{17} and $AuAg_{16}$ crystals (Supplementary Fig. 17). These interactions create rigid order in the crystals giving rise to a crystallization-induced emission. Enhanced emission by crystallization and lowering the temperature was reported for gold, silver and their alloy clusters[27,80,81]. $Ag_{13}Cu_4$ and $AuAg_{12}Cu_4$ exhibit emission bands at 650 and 610 nm, respectively, in solution (Fig. 6c, d). These clusters showed broad excitations ranging from 380-470 nm with a peak at 380 nm (Supplementary Figs. 45, 46). Bright luminescence was observed for the crystals of $Ag_{13}Cu_4$ and $AuAg_{12}Cu_4$ (Supplementary Fig. 47). Au incorporation in the core ($AuAg_{16}$) did not intensify the luminescence in solution, however the incorporation of Cu (for $Ag_{13}Cu_4$ cluster) in the outer shell significantly enhanced the luminescence intensity in solution. Similarly, the trimetallic $AuAg_{12}Cu_4$ cluster with both the core and the shell incorporation showed strong emission in solution. The emission behaviour of Ag_{17} NCs upon heteroatom doping can be compared with $Ag_{29}(S\text{-}Adm)_{18}(PPh_3)_4$ (where S-Adm is the adamantane
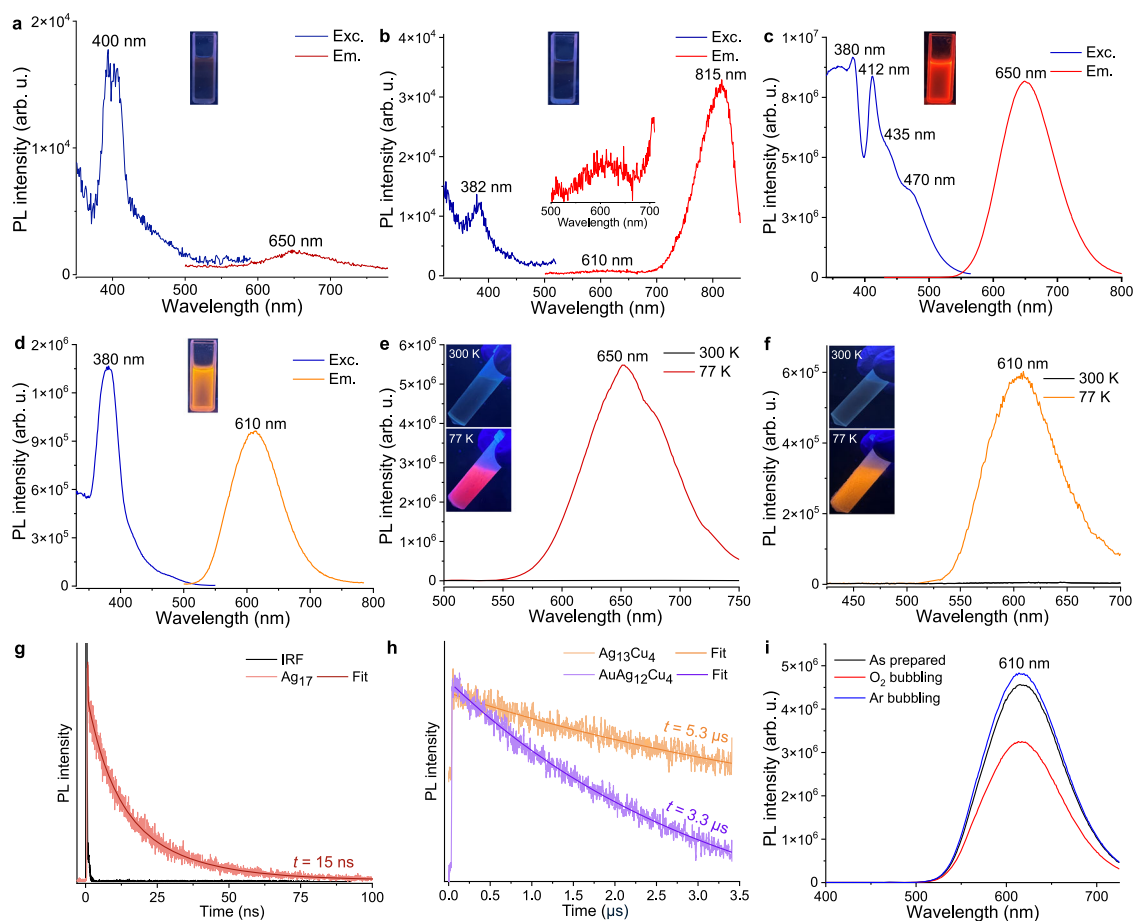
Fig. 6 | Photoluminescence spectra, emission enhancements, and decay profiles of Ag_{17}, $AuAg_{16}$, $Ag_{13}Cu_4$ and $AuAg_{12}Cu_4$ clusters. Photoluminescence excitation and emission spectra of **a** Ag_{17}, **b** $AuAg_{16}$, **c** $Ag_{13}Cu_4$ and **d** $AuAg_{12}Cu_4$ in DCM solution. Each inset shows the photograph of the respective cluster solution under a UV lamp at 365 nm. Solidification-induced emission enhancement of **e** Ag_{17} and **f** $AuAg_{16}$ clusters achieved by cooling the solution to 77 K. Inset shows the respective photographs of the solution at different temperatures. Luminescence decay profiles of **g** Ag_{17}, **h** $Ag_{13}Cu_4$ and $AuAg_{12}Cu_4$ clusters with average lifetimes. **i** PL intensity of $AuAg_{12}Cu_4$ cluster after exposure to oxygen and argon in DCM solution.

mercaptan) NCs, where luminescence was modulated based on the dopant type and its specific atomic position. In Ag_{29}, Au doping enhances luminescence, while Cu incorporation reduced it. However, in Ag_{17}, Cu doping at the shell ($Ag_{13}Cu_4$ and $AuAg_{12}Cu_4$) significantly increased the luminescence. These effects highlight the complex role of heteroatom positioning in modulating optical properties[82].

To understand the nature of the emissive excited states, luminescence decay measurements were performed. TCSPC measurement showed three component decay for Ag_{17} in DCM solution, having an average lifetime of 15 ns. Such decay is associated with a singlet excited state (Fig. 6g). On the other hand, Au and Cu incorporation significantly enhances the emissive lifetime (0.64 μs for $AuAg_{16}$ with two component decay and 5.3 μs for $Ag_{13}Cu_4$ with one component decay, see Supplementary Fig. 48 and Fig. 6h, respectively). Such a microsecond lifetime indicates phosphorescence emission, originating from the triplet states. Trimetallic $AuAg_{12}Cu_4$ cluster also showed phosphorescence emission with an average lifetime of 3.3 μs with one component decay (Fig. 6h). To further understand, oxygenation studies were performed upon exposing the cluster to oxygen gas. We observed significant quenching of luminescence intensity for $Ag_{13}Cu_4$ and trimetallic clusters after oxygen bubbling as depicted in Supplementary Fig. 49 and Fig. 6i, which further proved the presence of triplet excited states. Quenching of the emission intensity upon oxygen exposure confirmed the presence of triplet excited state for metal clusters[78].

Photophysics from TA spectroscopy

To understand the effect of heteroatoms on carrier dynamics of NCs, we performed fs TA spectroscopy on all the four NCs. We recorded the TA spectra (ΔA) of these NCs across the range of 440–650 nm at various pump-probe delay times, utilizing a 400 nm pump excitation with a pulse duration of 120 fs and a fluence of 350 μJ cm⁻². The results are presented in Fig. 7a–h. The TA spectrum of Ag_{17} (Fig. 7a) shows a broad featureless photoinduced absorption spanning from 440 to 640 nm, which grows continuously up to ≈1 ps before saturating and then starts to decay (Fig. 7b). This photoinduced absorption feature that shows a decay is not predicted by our theoretical calculations or observed in the optical absorption spectrum, suggesting its origin to the excited state absorption (ESA) of the NCs. ≈50% of 600 nm and ≈20% of 490 nm of ESA decays within 1 ns (Fig. 7b), indicating a differential relaxation process in Ag_{17}. In contrast, bimetallic $AuAg_{16}$ reached ESA saturation at ≈0.5 ps, and displayed a slower decay than Ag_{17} (Fig. 7c, d).

In contrast, the ESA of $Ag_{13}Cu_4$ shows continuous growth by many orders of magnitude compared to Ag_{17} and $AuAg_{16}$ without any observable saturation up to 1.5 ns (Fig. 7e, f), which is the limit of our experiment. This response starkly differs in the trimetallic $AuAg_{12}Cu_4$, which demonstrates a growth pattern up to 10 ps followed by a slower decay, providing a mixed response between the bimetallic $AuAg_{16}$ and $Ag_{13}Cu_4$ (Fig. 7g, h). To probe further into nanosecond timescales, flash photolysis experiments were conducted using a 355 nm, 7 ns pump excitation. Decay kinetics at 400 nm were best described by a single
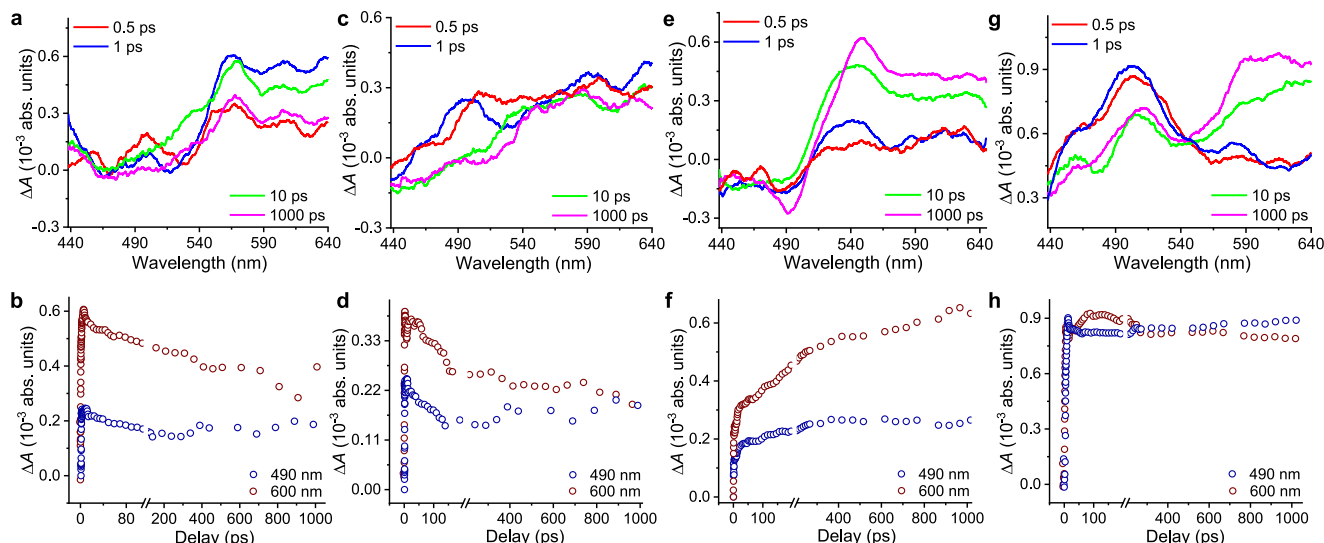
Fig. 7 | Fs TA spectra and decay kinetics of Ag$_{17}$, AuAg$_{16}$, Ag$_{13}$Cu$_4$ and AuAg$_{12}$Cu$_4$ clusters. Fs TA of the NCs at a fluence of 350 µJ cm^{-2}, at a 120 fs duration pump at 400 nm and different pump-probe delay times. The TA spectrum of **a** Ag$_{17}$, **c** AuAg$_{16}$, **e** Ag$_{13}$Cu$_4$, and **g** AuAg$_{12}$Cu$_4$. Decay kinetics at selected wavelengths for **b** Ag$_{17}$, **d** AuAg$_{16}$, **f** Ag$_{13}$Cu$_4$, and **h** AuAg$_{12}$Cu$_4$.

exponential function with a decay constant of ≈11 µs, indicating longer stability of the photo-excited carriers (Supplementary Fig. 50a). At 560 nm, the decay was too fast to capture, suggesting faster dynamics at this wavelength. TA decay profiles for AuAg$_{12}$Cu$_4$ demonstrated the short lifetime of carriers that is also described with single exponential decay kinetics having a decay constant of ≈6 ns (Supplementary Fig. 50b). The obtained lifetime of excited carriers follow the pattern similar to the PL lifetime, where also we saw the long lifetime of carriers upon introduction of the Cu atoms in the NCs. Comprehensively, the PL enhancement in bi and tri-metallic NCs appeared due to increased heteronuclearity and polarizability of metal-metal bonds[60,83]. The doping of Cu and Au into the Ag$_{17}$ cluster is likely to introduces relativistic effects where Au produces more pronounced effects compared to Cu in the electronic structure[84]. These relativistic effects are likely to alter orbital energies and electronic configurations, which can modulate the electronic states and optical characteristics of the NCs. This modulation may create more favorable conditions for intersystem crossing[85], ultimately leading to the observed extended decay lifetimes and enhanced phosphorescence in our Cu and Au-doped NCs.

Discussion

In this study, we explored the synergy of different metal atoms within atomically precise M$_{17}$ NCs, with a M@M$_{12}$@M$_4$ structure, exhibiting unique photophysical properties, protected with *ortho*-carborane-1-thiol (*o*$_1$-CBT). The parent Ag$_{17}$ cluster has a central icosahedral (Ag$_{13}$) core encapsulated by four capped Ag atoms. For bimetallic clusters, Au atoms occupies the central position of the icosahedron and resulted in the centrally Au incorporated Au@Ag$_{16}$, while four Cu atoms prefer the outer tetrahedral positions, and thus resulted in Ag$_{13}$@Cu$_4$. Incorporation of both Au and Cu atoms at their respective preferred positions lead to the formation of the trimetallic Au@Ag$_{12}$@Cu$_4$. All these clusters were stabilized by twelve carborane-thiol ligands. Molecular composition and structure of these clusters were revealed by mass spectrometry and SC-XRD structural analysis. Site-specific incorporation of Au and Cu in the M$_{17}$ NCs was supported by theoretical calculations. Alloying stabilizes the bimetallic clusters, rigidifies the cluster core, which was supported by computations and it leads to the opening up of the HOMO-LUMO gap. The Ag$_{17}$ displays fluorescence emission. Au incorporation provides slight stabilization to the emissive excited state, whereas Cu incorporation significantly enhances the decay lifetimes and resulted in phosphorescence emission. Theoretical calculations revealed that the central

atom incorporation of the cluster with a Au expands the HOMO-LUMO band gap in both AuAg$_{16}$ and AuAg$_{12}$Cu$_4$, whereas Cu incorporation to the outer capping region enhances photoluminescence emission in Ag$_{13}$Cu$_4$ and AuAg$_{12}$Cu$_4$. Fs TA showed structure specific relaxation of the excited state carriers. Altogether, this work explores the systematic site specific alloying leading to the synthesis of a carborane-thiol-protected trimetallic NC. It can also play a role to prepare diverse types of atomically precise photoemitters upon specific placement of a selective metal atom. Outer kernel substituted with Cu, bright luminescence and the packing pores of the trimetallic cluster in the solid state may lead to new catalysts, sensors and nano traps, especially considering the stability of these clusters.

Methods

Chemicals

Silver nitrate (AgNO$_3$, 99.0%) was purchased from Rankem Chemicals, while copper(I) chloride (CuCl, 97.0%), chloroauric acid (HAuCl$_4$, 98.0%), sodium borohydride (NaBH$_4$, 98.0%), 1,2-bis(diphenylphosphino)ethane (DPPE, 98.0%), and triphenylphosphine (TPP, 98.0%) were purchased from Sigma Aldrich. *Ortho*-carborane-1-thiol (*o*$_1$-CBT) was synthesized from *ortho*-carborane derivative, purchased from Katchem, Czech Republic. Crystalline *o*$_1$-CBT ligands (98.9%) were used for the NC synthesis. High-performance liquid chromatography (HPLC)-grade solvents, including dichloromethane (DCM, 99.8%), chloroform (CHCl$_3$, 99.4%), *n*-hexane (99.0%), acetonitrile (ACN, 99.8%), and methanol (MeOH, 99.5%), were sourced from Rankem Chemicals and Finar, India. Milli-Q water was used for cluster synthesis and purification. All the chemicals were commercially available and used without further purification.

Synthesis of Ag$_{17}$

The Ag$_{17}$ was synthesized at ice cold condition (≈ 0 °C) using a DPPE-assisted silver-thiolate co-reduction reaction. In brief, 20 mg AgNO$_3$ was dissolved in 5 mL of MeOH. 10 mg of *o*$_1$-CBT ligand was dissolved in 9 mL DCM, which was added in stirring condition. After 5 min of the reaction, 10 mg of DPPE, dissolved in 1 mL DCM was added to the reaction mixture. After 15 min of reaction, 20 mg NaBH$_4$, dissolved in 1 mL water, was added. A brownish solution was formed, which eventually converted to a dark brown solution after overnight reaction. After 18 h of reaction, the mixture was thoroughly washed with MeOH/H$_2$O followed by complete solvent evaporation. Then the cluster was

extracted using DCM and dried on a rotavapor. The yield of the product is 78% in terms of silver. Hexagonal single crystals were grown after 10 days at 4 °C through hexane vapor diffusion into the concentrated DCM solution (20 mg mL^{-1}) of the cluster.

Synthesis of bimetallic AuAg$_{16}$ and Ag$_{13}$Cu$_4$

To synthesize the bimetallic NCs AuAg$_{16}$ and Ag$_{13}$Cu$_4$, a similar synthetic procedure was employed. For the AuAg$_{16}$, a starting reagent consisting of 20 mg AgNO$_3$ and 5 mg of HAuCl$_4$ was utilized. On the other hand, for Ag$_{13}$Cu$_4$, a starting reagent containing 20 mg AgNO$_3$ and 20 mg of CuCl was used. Following a reaction time of 18 h, the resulting AuAg$_{16}$ NC exhibited a greenish-brown solution in DCM. On the other hand, Ag$_{13}$Cu$_4$ cluster gave an orange-brown color. Both the clusters were purified by thoroughly washing with MeOH/H$_2$O followed by complete solvent evaporation with final extraction in DCM. The yield of AuAg$_{16}$ and Ag$_{13}$Cu$_4$, measured in terms of silver content, was 65% and 72%, respectively. Rod-shaped yellowish-orange Ag$_{13}$Cu$_4$ crystals were grown by allowing hexane vapor diffusion into a concentrated solution in DCM/CHCl$_3$ mixture (1:1). After multiple efforts, cuboid crystals of AuAg$_{16}$ were grown in the DCM/ACN mixture (4:1), layered with hexane.

Synthesis of trimetallic AuAg$_{12}$Cu$_4$

The synthesis of the AuAg$_{12}$Cu$_4$ with three different metals was carried out using a similar procedure. To conduct the synthesis, a mixture consisting of 20 mg of AgNO$_3$, 5 mg of HAuCl$_4$, and 20 mg of CuCl was employed. The reaction took place for 18 h at 0 °C, followed by overnight standing at 4 °C. Formation of the trimetallic NC had a low yield of 35%-40% (measured in terms of silver). By allowing the as-synthesized mixture in a solution of DCM and MeOH to slowly evaporate at 4 °C, beautiful orange-colored polyhedral trimetallic crystals were obtained. The resulting trimetallic AuAg$_{12}$Cu$_4$ from the crystallization process was utilized for further studies.

Characterisations

All UV-vis absorption data were obtained on a Perkin Elmer Lambda 365 spectrophotometer at room temperature. The SC-XRD data was measured at temperatures ($T = 173$ or 296 K), using a Bruker D8 VENTURE diffractometer equipped with Cu K_α ($\lambda = 1.54178$ Å) radiation source and PHOTON II detector. The structure was solved by SHELXT-2018 and refined by full-matrix least squares techniques using SHELXL-2018 or 2019 software packages incorporated in WingX suite. High-resolution mass spectrometry employed a Waters Synapt G2-Si instrument for electrospray ionization and collision-induced dissociation studies. Photoluminescence properties of the nanoclusters in DCM/MeOH were recorded by a Horiba Jobin Yvon Nanolog, using a 450 W xenon-arc lamp source. TA spectrometer generate 120 fs pulses centered at 800 nm by Spectra physics Mai-Tai oscillator which are sent to Spectra physics Spitfire amplifier to generate high energy (4 mJ pulse^{-1}) 120 fs pulses with a repetition rate of 1 kHz. Differential pulse voltammetry measured a 2.04 eV band gap for Ag$_{17}$ clusters, aligning closely with theoretical predictions, though carborane-thiol protection caused electrode fouling, limiting further experiments.

DFT calculations. The DFT calculations were done using the GPAW software. The Kohn-Sham problem was solved by using real-space grids with 0.2 Å grid spacing. The electron-electron exchange-correlation interaction was approximated using the Perdew-Burke-Ernzerhof functional. Structure optimization started from the resolved crystal structures for each cluster type, and we used 0.05 eV/Å^{-1} maximum force limit for convergence. Symmetries of the frontier orbitals were analyzed using projections to spherical harmonics with respect to cluster's center of mass with 12.0 Å cutoff. LR-TDDFT was used for absorption spectra, dipole transition contribution map (DTCM) was used for analyzing the origin of the absorption peaks, and electron density oscillations of the peaks were visualized by using induced densities.

References

1. Chakraborty, I. & Pradeep, T. Atomically Precise Clusters of Noble Metals: Emerging Link between Atoms and Nanoparticles. *Chem. Rev.* **117**, 8208–8271 (2017).
2. Takano, S. & Tsukuda, T. Chemically Modified Gold/Silver Superatoms as Artificial Elements at Nanoscale: Design Principles and Synthesis Challenges. *J. Am. Chem. Soc.* **143**, 1683–1698 (2021).
3. Lee, S. et al. [Pt2Cu34(PET)22Cl4]2−: An Atomically Precise, 10-Electron PtCu Bimetal Nanocluster with a Direct Pt–Pt Bond. *J. Am. Chem. Soc.* **143**, 12100–12107 (2021).
4. Jin, R., Zeng, C., Zhou, M. & Chen, Y. Atomically Precise Colloidal Metal Nanoclusters and Nanoparticles: Fundamentals and Opportunities. *Chem. Rev.* **116**, 10346–10413 (2016).
5. Desireddy, A. et al. Ultrastable silver nanoparticles. *Nature* **501**, 399–402 (2013).
6. Gan, Z., Xia, N. & Wu, Z. Discovery, Mechanism, and Application of Antigalvanic Reaction. *Acc. Chem. Res.* **51**, 2774–2783 (2018).
7. Bootharaju, M. S., Joshi, C. P., Parida, M. R., Mohammed, O. F. & Bakr, O. M. Templated Atom-Precise Galvanic Synthesis and Structure Elucidation of a [Ag24Au(SR)18]− Nanocluster. *Angew. Chem. Int. Ed* **55**, 922–926 (2016).
8. Takano, S., Ito, S. & Tsukuda, T. Efficient and Selective Conversion of Phosphine-Protected (MAu8)2+ (M = Pd, Pt) Superatoms to Thiolate-Protected (MAu12)6+ or Alkynyl-Protected (MAu12)4+ Superatoms via Hydride Doping. *J. Am. Chem. Soc.* **141**, 15994–16002 (2019).
9. Fan, X. et al. Structural Isomerization in Cu(I) Clusters: Tracing the Cu Thermal Migration Paths and Unveiling the Structure-Dependent Photoluminescence. *CCS Chem.* https://doi.org/10.31635/ccschem.022.202101741 (2023).
10. Han, B.-L. et al. Polymorphism in Atomically Precise Cu23 Nanocluster Incorporating Tetrahedral [Cu4]O Kernel. *J. Am. Chem. Soc.* **142**, 5834–5841 (2020).
11. Sakthivel, N. A. & Dass, A. Aromatic Thiolate-Protected Series of Gold Nanomolecules and a Contrary Structural Trend in Size Evolution. *Acc. Chem. Res.* **51**, 1774–1783 (2018).
12. Gell, L., Lehtovaara, L. & Häkkinen, H. Superatomic S2 Silver Clusters Stabilized by a Thiolate–Phosphine Monolayer: Insight into Electronic and Optical Properties of Ag14(SC6H3F2)12(PPh3)8 and Ag16(SC6H3F2)14(DPPE)4. *J. Phys. Chem. A* **118**, 8351–8355 (2014).
13. Kang, X. & Zhu, M. Tailoring the photoluminescence of atomically precise nanoclusters. *Chem. Soc. Rev.* **48**, 2422–2457 (2019).
14. Abbas, M. A., Kamat, P. V. & Bang, J. H. Thiolated Gold Nanoclusters for Light Energy Conversion. *ACS Energy Lett* **3**, 840–854 (2018).
15. Huang, R.-W. et al. Radioluminescent Cu–Au Metal Nanoclusters: Synthesis and Self-Assembly for Efficient X-ray Scintillation and Imaging. *J. Am. Chem. Soc.* **145**, 13816–13827 (2023).
16. Russier-Antoine, I. et al. Ligand-core NLO-phores: a combined experimental and theoretical approach to the two-photon absorption and two-photon excited emission properties of small-ligated silver nanoclusters. *Nanoscale* **9**, 1221–1228 (2017).
17. Zhang, C., Si, W.-D., Wang, Z., Tung, C.-H. & Sun, D. Chiral Ligand-Concentration Mediating Asymmetric Transformations of Silver Nanoclusters: NIR-II Circularly Polarized Phosphorescence Lighting. *Angew. Chem. Int. Ed.* **63**, e202404545 (2024).
18. Zhang, M.-M. et al. Chiral Hydride Cu18 Clusters Transform to Superatomic Cu15Ag4 Clusters: Circularly Polarized Luminescence Lighting. *J. Am. Chem. Soc.* **145**, 22310–22316 (2023).

19. Qian, S. et al. Engineering luminescent metal nanoclusters for sensing applications. *Coord. Chem. Rev.* **451**, 214268 (2022).

20. Liu, C. et al. Chiral Ag23 nanocluster with open shell electronic structure and helical face-centered cubic framework. *Nat. Commun.* **9**, 744 (2018).

21. Nguyen, T.-A. D. et al. A Cu25 Nanocluster with Partial Cu(0) Character. *J. Am. Chem. Soc.* **137**, 13319–13324 (2015).

22. Chiu, T.-H. et al. Homoleptic Platinum/Silver Superatoms Protected by Dithiolates: Linear Assemblies of Two and Three Centered Icosahedra Isolobal to Ne2 and I3. *J. Am. Chem. Soc.* **141**, 12957–12961 (2019).

23. Bootharaju, M. S. et al. Cd12Ag32(SePh)36: Non-Noble Metal Doped Silver Nanoclusters. *J. Am. Chem. Soc.* **141**, 8422–8425 (2019).

24. Dhayal, R. S., van Zyl, W. E. & Liu, C. W. Polyhydrido Copper Clusters: Synthetic Advances, Structural Diversity, and Nanocluster-to-Nanoparticle Conversion. *Acc. Chem. Res.* **49**, 86–95 (2016).

25. Qu, M. et al. Observation of Non-FCC Copper in Alkynyl-Protected Cu53 Nanoclusters. *Angew. Chem. Int. Ed.* **59**, 6507–6512 (2020).

26. Kang, X., Li, Y., Zhu, M. & Jin, R. Atomically precise alloy nanoclusters: syntheses, structures, and properties. *Chem. Soc. Rev.* **49**, 6443–6514 (2020).

27. Khatun, E. et al. Confining an Ag10 Core in an Ag12 Shell: A Four-Electron Superatom with Enhanced Photoluminescence upon Crystallization. *ACS Nano* **13**, 5753–5759 (2019).

28. Nguyen, T.-A. D. et al. Ligand-Exchange-Induced Growth of an Atomically Precise Cu29 Nanocluster from a Smaller Cluster. *Chem. Mater.* **28**, 8385–8390 (2016).

29. Jana, A. et al. A luminescent Cu 4 cluster film grown by electrospray deposition: a nitroaromatic vapour sensor. *Nanoscale* **15**, 8141–8147 (2023).

30. Wang, Q.-Y. et al. o-Carborane-Based and Atomically Precise Metal Clusters as Hypergolic Materials. *J. Am. Chem. Soc.* **142**, 12010–12014 (2020).

31. Huang, J.-H., Ji, A.-Q., Wang, Z.-Y., Wang, Q.-Y. & Zang, S.-Q. Boosting 2000-Fold Hypergolic Ignition Rate of Carborane by Substitutes Migration in Metal Clusters. *Adv. Sci.* **11**, 2401861 (2024).

32. Jana, A. et al. Light-Activated Intercluster Conversion of an Atomically Precise Silver Nanocluster. *ACS Nano* **15**, 15781–15793 (2021).

33. Wang, J., Wang, Z.-Y., Li, S.-J., Zang, S.-Q. & Mak, T. C. W. Carboranealkynyl-Protected Gold Nanoclusters: Size Conversion and UV/Vis–NIR Optical Properties. *Angew. Chem.* **133**, 6024–6029 (2021).

34. Wang, J., Xu, F., Wang, Z.-Y., Zang, S.-Q. & Mak, T. C. W. Ligand-Shell Engineering of a Au28 Nanocluster Boosts Electrocatalytic CO2 Reduction. *Angew. Chem. Int. Ed.* **61**, e202207492 (2022).

35. Jana, A. et al. Carboranethiol-Protected Propeller-Shaped Photo-responsive Silver Nanomolecule. *Inorg. Chem.* **61**, 8593–8603 (2022).

36. Morin, J.-F., Shirai, Y. & Tour, J. M. En Route to a Motorized Nanocar. *Org. Lett.* **8**, 1713–1716 (2006).

37. Goronzy, D. P. et al. Influence of Terminal Carboxyl Groups on the Structure and Reactivity of Functionalized m-Carboranethiolate Self-Assembled Monolayers. *Chem. Mater.* **32**, 6800–6809 (2020).

38. Wang, J. et al. Carborane Derivative Conjugated with Gold Nanoclusters for Targeted Cancer Cell Imaging. *Biomacromolecules* **18**, 1466–1472 (2017).

39. Fisher, S. P. et al. Nonclassical Applications of closo-Carborane Anions: From Main Group Chemistry and Catalysis to Energy Storage. *Chem. Rev.* **119**, 8262–8290 (2019).

40. Poater, J. et al. Too Persistent to Give Up: Aromaticity in Boron Clusters Survives Radical Structural Changes. *J. Am. Chem. Soc.* **142**, 9396–9407 (2020).

41. White, K. E. et al. Competing Intermolecular and Molecule–Surface Interactions: Dipole–Dipole-Driven Patterns in Mixed Carborane Self-Assembled Monolayers. *Chem. Mater.* **36**, 2085–2095 (2024).

42. Huang, J.-H., Wang, Z.-Y., Zang, S.-Q. & Mak, T. C. W. Spontaneous Resolution of Chiral Multi-Thiolate-Protected Ag30 Nanoclusters. *ACS Cent. Sci.* **6**, 1971–1976 (2020).

43. Ghosh, A., Mohammed, O. F. & Bakr, O. M. Atomic-Level Doping of Metal Clusters. *Acc. Chem. Res.* **51**, 3094–3103 (2018).

44. Kim, M. et al. Dopant-Dependent Electronic Structures Observed for M2Au36(SC6H13)24 Clusters (M = Pt, Pd). *J. Phys. Chem. Lett.* **9**, 982–989 (2018).

45. Choi, W. et al. Effects of Metal-Doping on Hydrogen Evolution Reaction Catalyzed by MAu24 and M2Au36 Nanoclusters (M = Pt, Pd). *ACS Appl. Mater. Interf.* **10**, 44645–44653 (2018).

46. Xie, S., Tsunoyama, H., Kurashige, W., Negishi, Y. & Tsukuda, T. Enhancement in Aerobic Alcohol Oxidation Catalysis of Au25 Clusters by Single Pd Atom Doping. *ACS Catal* **2**, 1519–1523 (2012).

47. Chakrahari, K. K. et al. Synthesis of Bimetallic Copper-Rich Nanoclusters Encapsulating a Linear Palladium Dihydride Unit. *Angew. Chem. Int. Ed.* **58**, 4943–4947 (2019).

48. Bootharaju, M. S. et al. Atom-Precise Heteroatom Core-Tailoring of Nanoclusters for Enhanced Solar Hydrogen Generation. *Adv. Mater.* **35**, 2207765 (2023).

49. Masuda, S., Sakamoto, K. & Tsukuda, T. Atomically precise Au and Ag nanoclusters doped with a single atom as model alloy catalysts. *Nanoscale* **16**, 4514–4528 (2024).

50. Chen, S. et al. Assembly of the Thiolated [Au1Ag22(S-Adm)12]3+ Superatom Complex into a Framework Material through Direct Linkage by SbF6– Anions. *Angew. Chem.* **132**, 7612–7617 (2020).

51. Du, W. et al. Ag50(Dppm)6(SR)30 and Its Homologue AuxAg50–x(Dppm)6(SR)30 Alloy Nanocluster: Seeded Growth, Structure Determination, and Differences in Properties. *J. Am. Chem. Soc.* **139**, 1618–1624 (2017).

52. Chai, J. et al. Chiral Inversion and Conservation of Clusters: A Case Study of Racemic Ag32Cu12 Nanocluster. *Inorg. Chem.* **60**, 9050–9056 (2021).

53. Kim, M. et al. Insights into the Metal-Exchange Synthesis of MAg24(SR)18 (M = Ni, Pd, Pt) Nanoclusters. *Chem. Mater.* **32**, 10216–10226 (2020).

54. Khatun, E. & Pradeep, T. New Routes for Multicomponent Atomically Precise Metal Nanoclusters. *ACS Omega* **6**, 1–16 (2021).

55. Yan, J. et al. Total Structure and Electronic Structure Analysis of Doped Thiolated Silver [MAg24(SR)18]2– (M = Pd, Pt) Clusters. *J. Am. Chem. Soc.* **137**, 11880–11883 (2015).

56. Yang, Y. et al. An All-Alkynyl Protected 74-Nuclei Silver(I)–Copper(I)-Oxo Nanocluster: Oxo-Induced Hierarchical Bimetal Aggregation and Anisotropic Surface Ligand Orientation. *Angew. Chem. Int. Ed.* **58**, 12280–12285 (2019).

57. He, L. et al. Kernel Tuning and Nonuniform Influence on Optical and Electrochemical Gaps of Bimetal Nanoclusters. *J. Am. Chem. Soc.* **140**, 3487–3490 (2018).

58. Hossain, S. et al. Thiolate-Protected Trimetallic Au~20Ag~4Pd and Au~20Ag~4Pt Alloy Clusters with Controlled Chemical Composition and Metal Positions. *J. Phys. Chem. Lett.* **9**, 2590–2594 (2018).

59. Han, B.-L. et al. Precise Implantation of an Archimedean Ag@Cu12 Cuboctahedron into a Platonic Cu4Bis(diphenylphosphino)hexane6 Tetrahedron. *ACS Nano* **15**, 8733–8741 (2021).

60. Xie, X.-Y. et al. The Origin of the Photoluminescence Enhancement of Gold-Doped Silver Nanoclusters: The Importance of Relativistic Effects and Heteronuclear Gold–Silver Bonds. *Angew. Chem. Int. Ed.* **57**, 9965–9969 (2018).

61. Hirai, H. et al. Doping-Mediated Energy-Level Engineering of M@Au12 Superatoms (M=Pd, Pt, Rh, Ir) for Efficient Photoluminescence and Photocatalysis. *Angew. Chem. Int. Ed.* **61**, e202207290 (2022).

62. Fakhouri, H. et al. Effects of Single Platinum Atom Doping on Stability and Nonlinear Optical Properties of Ag29 Nanoclusters. *J. Phys. Chem. C* **126**, 21094–21100 (2022).

63. Yuan, S.-F., Guan, Z.-J., Liu, W.-D. & Wang, Q.-M. Solvent-triggered reversible interconversion of all-nitrogen-donor-protected silver nanoclusters and their responsive optical properties. *Nat. Commun.* **10**, 4032 (2019).

64. Chevrier, D. M. et al. Interactions between Ultrastable Na4Ag44(SR) 30 Nanoclusters and Coordinating Solvents: Uncovering the Atomic-Scale Mechanism. *ACS Nano* **14**, 8433–8441 (2020).

65. Udayabhaskararao, T. & Pradeep, T. New Protocols for the Synthesis of Stable Ag and Au Nanocluster Molecules. *J. Phys. Chem. Lett.* **4**, 1553–1564 (2013).

66. Manno, R. et al. Continuous Microwave-Assisted Synthesis of Silver Nanoclusters Confined in Mesoporous SBA-15: Application in Alkyne Cyclizations. *Chem. Mater.* **32**, 2874–2883 (2020).

67. Bootharaju, M. S. et al. Reversible Size Control of Silver Nanoclusters via Ligand-Exchange. *Chem. Mater.* **27**, 4289–4297 (2015).

68. Yuan, X. et al. Traveling through the Desalting Column Spontaneously Transforms Thiolated Ag Nanoclusters from Nonluminescent to Highly Luminescent. *J. Phys. Chem. Lett.* **4**, 1811–1815 (2013).

69. Wickramasinghe, S. et al. M3Ag17(SPh)12 Nanoparticles and Their Structure Prediction. *J. Am. Chem. Soc.* **137**, 11550–11553 (2015).

70. Conn, B. E. et al. Confirmation of a de novo structure prediction for an atomically precise monolayer-coated silver nanoparticle. *Sci. Adv.* **2**, e1601609 (2016).

71. Jana, A. et al. Photoconversion of Ag31 to Ag42 Initiated by Solvated Electrons. *Chem. Mater.* **35**, 7020–7031 (2023).

72. Qu, M. et al. Bidentate Phosphine-Assisted Synthesis of an All-Alkynyl-Protected Ag74 Nanocluster. *J. Am. Chem. Soc.* **139**, 12346–12349 (2017).

73. Dhayal, R. S. et al. Ag21S2P(OiPr)212]+: An Eight-Electron Superatom. *Angew. Chem. Int. Ed.* **54**, 3702–3706 (2015).

74. Chang, W.-T. et al. Eight-Electron Silver and Mixed Gold/Silver Nanoclusters Stabilized by Selenium Donor Ligands. *Angew. Chem. Int. Ed.* **56**, 10178–10182 (2017).

75. Dhayal, R. S. et al. [Ag20S2P(OR)212]: A Superatom Complex with a Chiral Metallic Core and High Potential for Isomerism. *Chem. – Eur. J* **22**, 9943–9947 (2016).

76. Yen, W.-J., Liao, J.-H., Chiu, T.-H., Wen, Y.-S. & Liu, C. W. Homoleptic Silver-Rich Trimetallic M20 Nanocluster. *Inorg. Chem.* **61**, 6695–6700 (2022).

77. Zhong, Y.-J. et al. Doping effect on the structure and properties of eight-electron silver nanoclusters. *J. Chem. Phys.* **155**, 034304 (2021).

78. Jana, A. et al. Carborane-thiol protected copper nanoclusters: stimuli-responsive materials with tunable phosphorescence. *Chem. Sci.* **14**, 1613–1626 (2023).

79. Gam, F. et al. Alloying dichalcogenolate-protected Ag21 eight-electron nanoclusters: a DFT investigation. *Nanoscale* **14**, 196–203 (2021).

80. Liu, D. et al. [Au14(2-SAdm)9(Dppe)2]+: a gold nanocluster with a crystallization-induced emission enhancement phenomenon. *Chem. Commun.* **60**, 1337–1340 (2024).

81. Kang, X., Wang, S. & Zhu, M. Observation of a new type of aggregation-induced emission in nanoclusters. *Chem. Sci.* **9**, 3062–3068 (2018).

82. Kang, X. et al. Rational construction of a library of M29 nanoclusters from monometallic to tetrametallic. *Proc. Natl. Acad. Sci.* **116**, 18834–18840 (2019).

83. Galassi, R. et al. Cupriphication of gold to sensitize d10–d10 metal–metal bonds and near-unity phosphorescence quantum yields. *Proc. Natl. Acad. Sci.* **114**, E5042–E5051 (2017).

84. Häkkinen, H., Moseler, M. & Landman, U. Bonding in Cu, Ag, and Au Clusters: Relativistic Effects, Trends, and Surprises. *Phys. Rev. Lett.* **89**, 033401 (2002).

85. Song, Y. et al. Ultrabright Au@Cu14 nanoclusters: 71.3% phosphorescence quantum yield in non-degassed solution at room temperature. *Sci. Adv.* **7**, eabd2091 (2021).

Author contributions
V.Y. performed the synthesis, crystallization, and most of the experimental studies. A.J. and V.Y. performed structural characterization and photophysical studies. S.Ac. performed mass spectrometric studies. H.N. assisted V.Y. for synthetic scaleup. A.R.K. conducted electron microscopic and XPS measurements. All the fs–ns time-resolved studies were conducted by A.S. in the laboratory of K.N.V.D.A. S.M. and H.H. performed computational studies. J.M. and T.B. synthesized the carborane thiols used in this work and conducted all the work relating to those systems. Single-crystal X-ray structure refinement was done by S.An. The first draft of the manuscript was written by V.Y., and all the authors contributed to improving it. T.P. suggested the problem, supervised the project, and finalized the manuscript. This work is a part of longer-term collaboration aimed at unlocking the potential of materials produced by combining metal NCs and carborane ligands initiated by T.P. and T.B.

Competing interests
The authors declare no competing interests.

Additional information
Supplementary information The online version contains supplementary material available at
https://doi.org/10.1038/s41467-025-56385-w.

Correspondence and requests for materials should be addressed to Kumaran Nair Valsala Devi Adarsh, Tomas Base, Hannu Häkkinen or Thalappil Pradeep.

Peer review information *Nature Communications* thanks the anonymous reviewers for their contribution to the peer review of this work. A peer review file is available.

Reprints and permissions information is available at
http://www.nature.com/reprints